

Magnetic Imaging with Spin Defects in Hexagonal Boron Nitride

P. Kumar¹, F. Fabre,¹ A. Durand¹, T. Clua-Provost,¹ J. Li,² J.H. Edgar,² N. Rougemaille,³ J. Coraux,³ X. Marie,⁴ P. Renucci,⁴ C. Robert,⁴ I. Robert-Philip,¹ B. Gil,¹ G. Cassabois¹, A. Finco¹, and V. Jacques^{1,*}

¹Laboratoire Charles Coulomb, Université de Montpellier and CNRS, 34095 Montpellier, France

²Tim Taylor Department of Chemical Engineering, Kansas State University, Manhattan, Kansas 66506, USA

³Univ. Grenoble Alpes, CNRS, Grenoble INP, Institut Néel, 38000 Grenoble, France

⁴Université de Toulouse, INSA-CNRS-UPS, LPCNO, 135 Avenue Rangueil, 31077 Toulouse, France

(Received 21 July 2022; revised 17 October 2022; accepted 23 November 2022; published 21 December 2022)

Optically active spin defects hosted in hexagonal boron nitride (*h*-BN) are promising candidates for the development of a two-dimensional (2D) quantum sensing unit. Here, we demonstrate quantitative magnetic imaging with *h*-BN flakes doped with negatively charged boron-vacancy (V_B^-) centers through neutron irradiation. As a proof-of-concept, we image the magnetic field produced by CrTe₂, a van der Waals ferromagnet with a Curie temperature slightly above 300 K. Compared to other quantum sensors embedded in 3D materials, the advantages of the *h*-BN-based magnetic sensor described in this work are its ease of use, high flexibility, and, more importantly, its ability to be placed in close proximity to a target sample. Such a sensing unit will likely find numerous applications in 2D materials research by offering a simple way to probe the physics of van der Waals heterostructures.

DOI: 10.1103/PhysRevApplied.18.L061002

Quantum sensing technologies based on solid-state spin defects have already shown huge potential to cover the growing need for high-precision sensors [1], both for fundamental research and for industrial applications. The most advanced quantum sensing platforms to date rely on optically active spin defects embedded in three-dimensional (3D) materials [2]. A prime example is the nitrogen-vacancy (N-V) center in diamond [3–5], which has already found a wide range of applications in condensed matter physics [6], life sciences [7], and geophysics [8]. Despite such success, N-V-based quantum sensing technologies still face several limitations that mainly result from the 3D structure of the diamond host matrix. These include (i) a limited proximity between the quantum sensor and the target sample, which hampers its sensitivity, and (ii) the inability to engineer ultrathin and flexible diamond layers, which precludes an easy transfer of the quantum sensing unit onto the samples to be probed as well as its integration into complex multifunctional devices. An emerging strategy to circumvent these limitations involves using spin defects embedded in a van der Waals crystal that could be exfoliated down to the monolayer limit [9,10]. Such a 2D quantum sensing foil could potentially offer atomic-scale proximity to the probed sample together with an increased versatility and flexibility for device integration.

Hexagonal boron nitride (*h*-BN) is currently the most promising van der Waals crystal for the design of quantum sensing foils [9,10]. This insulating material, which can be easily exfoliated down to few atomic layers while maintaining chemical stability, is extensively used for encapsulation of van der Waals heterostructures [11]. Furthermore, *h*-BN hosts a broad diversity of optically active point defects owing to its wide bandgap [12–15]. For some of these defects, the electron spin resonance (ESR) can be detected optically, offering a key resource for quantum sensing applications [9]. While several spin-active defects with unknown microscopic structures have recently been isolated at the single level in *h*-BN [16–18], most studies to date have been focused on ensembles of negatively charged boron-vacancy (V_B^-) centers [19] [Fig. 1(a)]. Under green laser illumination, this defect produces a broadband photoluminescence (PL) signal in the near infrared. In addition, the V_B^- center features magneto-optical properties very similar to those of the N-V defect in diamond, with a spin triplet ground state whose ESR frequencies can be measured via optically detected magnetic resonance methods [19,20]. Despite a low quantum yield that has so far prevented its optical detection at the single scale, ensembles of V_B^- centers have recently found applications as quantum sensors in van der Waals heterostructures [21,22].

In this work, we analyze the performance of *h*-BN flakes doped with V_B^- centers by neutron irradiation for

*vincent.jacques@umontpellier.fr

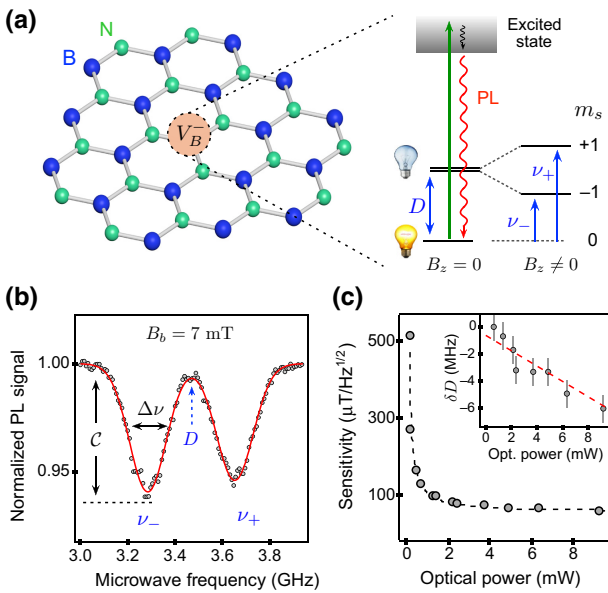


FIG. 1. (a) Atomic structure of the V_B^- center in $h\text{-BN}$ with a simplified diagram of its energy levels showing the ESR transitions ν_{\pm} in the spin triplet ground state. (b) Optically detected ESR spectrum recorded on a 85-nm-thick $h\text{-BN}$ flake with an out-of-plane bias field $B_b = 7$ mT and an optical power of 2.1 mW. The solid line is a fit to the data with Lorentzian functions. (c) Magnetic field sensitivity η_B as a function of the optical pumping power. The black dashed line is a guide to the eye. Inset: Evolution of δD with the optical power. The red dashed line is a fit to the data with a linear function.

quantitative magnetic field imaging. As a proof of concept, we image the magnetic field produced by 1T-CrTe₂, a van der Waals ferromagnet with in-plane magnetic anisotropy. In its bulk form, this crystal exhibits a Curie temperature (T_c) slightly above 300 K and a magnetization around $M \sim 130$ kA/m under ambient conditions [23–26]. Magnetic flakes with a thickness of a few tens of nanometers were obtained by mechanical exfoliation of a bulk 1T-CrTe₂ crystal and then transferred onto a SiO₂/Si substrate. For magnetic imaging, we rely on a monoisotopic $h\text{-BN}$ crystal grown from a Ni-Cr flux [27], which was irradiated with thermal neutrons with a dose of about 2.6×10^{16} n/cm² (n means neutron) (see [28]). The interest of isotopic purification with ¹⁰B lies in its very large neutron capture cross section, which ensures an efficient creation of V_B^- centers via neutron transmutation doping [29,30]. $h\text{-BN}$ flakes mechanically exfoliated from this neutron-irradiated crystal were deposited above the CrTe₂ flakes to form a van der Waals heterostructure. Besides providing magnetic imaging capabilities, the V_B^- -doped $h\text{-BN}$ capping layer also protects CrTe₂ from degradation of its magnetic properties. For each sample, the thickness of the different layers was inferred by atomic force microscopy (AFM).

All experiments described below are carried out under ambient conditions with a scanning confocal microscope

employing a green laser excitation, a high-numerical aperture microscope objective (NA = 0.7) and a photon counting detection module. At each point of the sample, optical illumination combined with microwave excitation enables the measurement of the ESR frequencies of the V_B^- center by recording its spin-dependent PL intensity [19]. In this work, the microwave excitation is delivered via an external loop antenna placed close to the sample.

We start by studying a heterostructure consisting of a 64-nm-thick CrTe₂ flake covered with a 85-nm-thick $h\text{-BN}$ sensing layer [see Fig. 2(a)]. Before discussing magnetic imaging results, we first qualify the magnetic field sensitivity of the V_B^- -doped $h\text{-BN}$ layer as a function of the optical excitation power. To this end, optically detected ESR spectra were recorded far from the CrTe₂ flake while applying a bias magnetic field $B_b = 7$ mT along the c axis of $h\text{-BN}$ (i.e., perpendicular to the layers). A typical spectrum is shown in Fig. 1(b). The ESR frequencies are given by $\nu_{\pm} = D \pm \gamma_e B_b$, where $\gamma_e = 28$ GHz/T is the electron gyromagnetic ratio and $D \sim 3.47$ GHz denotes the zero-field splitting parameter of the V_B^- spin triplet ground state [Fig. 1(a)]. From such a spectrum, the magnetic field sensitivity η_B can be inferred as [31]

$$\eta_B \approx 0.7 \times \frac{1}{\gamma_e} \times \frac{\Delta\nu}{\mathcal{C}\sqrt{\mathcal{R}}}, \quad (1)$$

where B is magnetic field, \mathcal{R} is the rate of detected photons, \mathcal{C} the contrast of the magnetic resonance, and $\Delta\nu$ its linewidth [Fig. 1(b)]. From the parameters $\{\mathcal{R}, \mathcal{C}, \Delta\nu\}$ measured at different optical powers, we extract the power-dependent magnetic field sensitivity. As shown in Fig. 1(c), η_B improves with increasing laser power and achieves an optimal value around 60 $\mu\text{T}/\sqrt{\text{Hz}}$. Note that in the power range considered, the PL signal does not reach saturation and the ESR linewidth $\Delta\nu$ remains almost constant (see [28]). The magnetic sensitivity is therefore mainly limited by the ESR contrast \mathcal{C} , which could be improved by optimizing the orientation of the microwave magnetic field, for example by depositing the $h\text{-BN}$ flakes on top of a coplanar waveguide [32].

Interestingly, the gain in sensitivity with optical power is accompanied by a slight reduction of the zero-field splitting parameter $D = (\nu_+ + \nu_-)/2$, whose relative shift δD is plotted in the inset of Fig. 1(c). This shift results from a temperature variation δT of the $h\text{-BN}$ layer [9,33], which can be phenomenologically described near room temperature by the relation $\delta D = \varepsilon \delta T$ where $\varepsilon \sim -0.7$ MHz/K [9]. Our measurements thus indicate that optical illumination leads to heating of the $h\text{-BN}$ sensing layer. Fitting the data with a linear function leads to an optically induced heating efficiency around 1 K/mW. To mitigate this effect, which is detrimental for studying the magnetic order in materials featuring a T_c near room temperature like CrTe₂, magnetic imaging experiments were carried out at low optical power

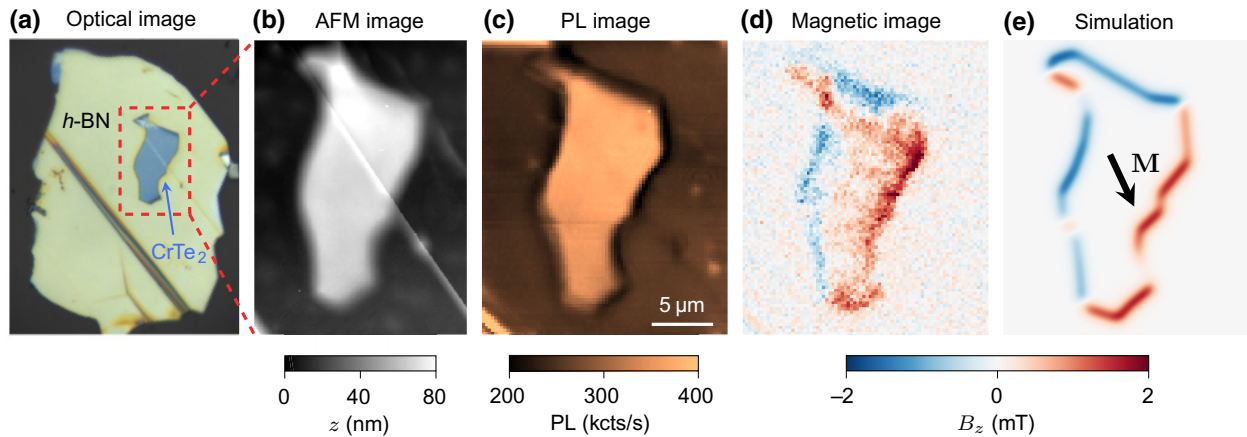


FIG. 2. (a) Optical image of the CrTe₂ (64 nm)/h-BN (85 nm) heterostructure. (b) AFM image indicating that the magnetic layer has a constant thickness. (c) PL image recorded across the same area as in (b). (d) Corresponding map of the magnetic field component B_z obtained by measuring the Zeeman shift of the lower ESR frequency of the V_B^- centers. Experiments are carried out with a bias magnetic field $B_b = 7$ mT and an optical power of 0.6 mW. The acquisition time per pixel is 4.2 s. (e) Simulated map of the magnetic field component B_z for a uniform in-plane magnetization \mathbf{M} (black arrow) with an azimuthal angle $\phi_M = 297^\circ$ and a norm $M = 60$ kA/m.

(around 0.6 mW), leading to a slightly degraded magnetic field sensitivity $\eta_B \sim 130$ $\mu\text{T}/\sqrt{\text{Hz}}$ [Fig. 1(c)].

A PL raster scan of the CrTe₂ (64 nm)/h-BN (85 nm) heterostructure is shown in Fig. 2(c). The increased PL signal above the CrTe₂ flake is related to its metallic character leading to reflection effects [32]. Magnetic field imaging is performed by recording an ESR spectrum at each point of the scan, from which the Zeeman shift of the lower ESR frequency ν_- is extracted. Here, we only track one magnetic resonance of the V_B^- center to reduce data acquisition time. After subtracting the offset linked to the bias magnetic field B_b , the Zeeman shift is simply given by $\Delta_z = \gamma_e B_z$, where B_z is the magnetic field projection along the V_B^- quantization axis, which corresponds to the c axis of h-BN. A map of the magnetic field component B_z produced by the CrTe₂ flake is shown in Fig. 2(d). The magnetic field is mainly generated at the edges of the flake as expected for a uniformly magnetized flake with homogeneous thickness [26]. Furthermore, the recorded magnetic field distribution directly confirms that the CrTe₂ flake features an in-plane magnetization. Indeed, considering a uniform out-of-plane magnetization, the magnetic field component B_z would be identical at all edges of the flake (see [28]).

To perform a quantitative analysis of the recorded magnetic map, we simulate the distribution of the magnetic field component B_z produced by a CrTe₂ flake with constant thickness and uniform in-plane magnetization \mathbf{M} . This vector is characterized by its azimuthal angle ϕ_M in the (x, y) sample plane and norm M . The geometry of the flake used for the simulation is extracted from a topography image recorded by AFM [Fig. 2(b)]. By comparing the overall structure of the experimental magnetic image with simulations obtained for various values of the angle ϕ_M ,

we first identify the magnetization orientation $\phi_M \sim 297^\circ$ [Fig. 2(e)]. Considering solely shape anisotropy, the in-plane magnetization should be stabilized along the long axis of the CrTe₂ flake. Our result indicates a deviation from this simple case, which suggests that CrTe₂ exhibits a nonnegligible magnetocrystalline anisotropy, in agreement with recent works [25,26].

Having identified the orientation of the magnetization vector, we then estimate its norm M by analyzing the stray field amplitude recorded at the edges of the CrTe₂ flake. Besides being linked to the magnetization norm, the Zeeman shift of the ESR frequency measured at each pixel of the scan also results from both (i) a lateral averaging due to the diffraction-limited spatial resolution of the magnetic microscope and (ii) an averaging over the vertical (z) distribution of optically active V_B^- centers in the h-BN sensing layer. Indeed, neutron irradiation creates V_B^- centers throughout the h-BN volume, in contrast to ion implantation techniques which lead to the creation of defects at a depth linked to the ion implantation energy [34,35]. Taking into account these two averaging processes (see [28]), fair agreement is obtained between the simulated and experimental magnetic maps for $M \sim 60$ kA/m [Fig. 2(e)]. This value is twice larger than the one recently measured for micron-sized CrTe₂ flakes without h-BN encapsulation [26]. This discrepancy is attributed to a partial degradation of nonencapsulated CrTe₂ flakes resulting in a reduced effective magnetization. However, the magnetization remains twice lower than that estimated for a bulk CrTe₂ crystal [23]. The origin of the difference is unknown so far, but could relate to significant variations of the Curie temperature induced by mechanical deformations during exfoliation, similar to observations on other

Cr-Te compounds [36]. As already indicated above, the magnetic image shown in Fig. 2(d) was recorded at a low optical excitation power to mitigate heating effects. The same experiments performed at larger optical powers show a weaker stray magnetic field at the edges of the flake (see [28]). Since CrTe_2 has a T_c close to room temperature, any slight heating of the sample significantly reduces the sample magnetization.

Next we study a heterostructure with a thinner top $h\text{-BN}$ sensing layer (15 nm) in order to rely on an ensemble of V_B^- centers localized closer to the CrTe_2 surface, thus reducing vertical averaging effects. An optical image of this second heterostructure is shown in Fig. 3(a). The magnetic field sensitivity of the 15-nm-thick $h\text{-BN}$ layer was first measured far from the CrTe_2 flake as a function of the optical pumping power, by following the procedure described above [see Eq. (1)]. We obtain a behavior similar to that observed for the 85-nm-thick $h\text{-BN}$ layer, with a magnetic sensitivity improving with increasing optical power, before reaching an optimal value $\eta_B \sim 110 \mu\text{T}/\sqrt{\text{Hz}}$ [Fig. 3(b)]. This value is worse than that obtained for the 85-nm-thick $h\text{-BN}$ flake due to a reduced ESR contrast and a lower rate of detected photons (see [28]). Once again, our measurements also indicate that optical illumination leads to heating of the $h\text{-BN}$ sensing layer [see inset of Fig. 3(b)].

A PL raster scan recorded around the CrTe_2 flake is shown in Fig. 3(c). While the PL signal was larger for a thick $h\text{-BN}$ layer deposited on CrTe_2 owing to reflection effects [see Fig. 2(c)], the PL scan of this second heterostructure now reveals a strong PL quenching of the V_B^- centers located above the magnetic layer. This effect also results from the metallic character of CrTe_2 . Indeed, when the V_B^- centers are placed in close proximity (less than 10 nm away) to the CrTe_2 flake, energy transfer to

the metal quenches their PL signal by opening additional nonradiative decay channels [37,38]. Even though such a PL quenching impairs the magnetic sensitivity of the $h\text{-BN}$ layer, magnetic imaging can still be performed by increasing the optical pumping power, which, however, induces sample heating [Fig. 3(e)]. Despite an improved proximity of the V_B^- centers, the overall amplitude of the stray magnetic field is not stronger than the one previously measured with a thicker $h\text{-BN}$ layer. This is due to laser-induced heating of the magnetic flake, which reduces its magnetization, as discussed above. We note that the shift of the ESR frequency then results both from the Zeeman effect and the temperature-induced variation of the zero-field splitting parameter (D). In principle it is possible to infer the temperature distribution independently by recording the two ESR frequencies of the V_B^- center at each point of the scan [21]. However, given the stability of our experimental setup, we can only track a single ESR frequency, thus reducing the data acquisition time and minimizing mechanical drifts.

For this second heterostructure, a quantitative analysis of the stray field distribution is a difficult task because of large variations of the CrTe_2 thickness. Indeed, a topography image recorded by AFM shows that the magnetic flake is divided into two main parts whose average thickness varies from about 115 nm to about 31 nm, with local fluctuations exceeding 20% due to wrinkles [Fig. 3(d)]. Since magnetic stray fields are produced at each thickness step of the magnetic layer with a possible reorientation of the in-plane magnetization [26], precise magnetic simulations can hardly be performed. Considering a simplified geometry of the CrTe_2 flake with a constant thickness (115 nm), the magnetic field produced at the top left-hand edge is reproduced for a magnetization $M \sim 40 \text{ kA/m}$.

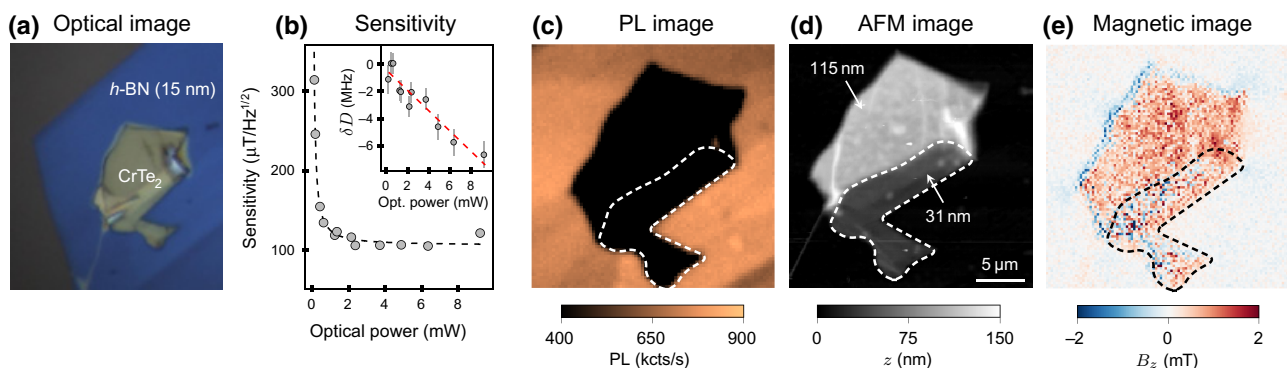


FIG. 3. (a) Optical image of a heterostructure consisting of a 15-nm-thick $h\text{-BN}$ layer deposited on top of a CrTe_2 flake. (b) Magnetic field sensitivity of the $h\text{-BN}$ layer as a function of the optical pumping power. The measurements are performed far from the CrTe_2 flake. Inset: Evolution of δD with the optical power. The red dashed line is a fit to the data with a linear function. (c) PL image recorded around the CrTe_2 flake. (d) AFM image of the CrTe_2 flake showing large thickness variations. (e) Corresponding map of the magnetic field component B_z obtained by measuring the Zeeman shift of the lower ESR frequency of the V_B^- centers. Experiments are carried out with a bias magnetic field $B_b = 7 \text{ mT}$ and an optical power of 2.4 mW. The acquisition time per pixel is 15.3 s. kcts/s, kilocounts per second.

Although qualitative, this analysis confirms the reduction of the magnetization induced by laser-induced heating of the magnetic layer.

In summary, we have shown that V_B^- spin defects hosted in *h*-BN layers can be used for quantitative magnetic imaging with a sensitivity around $100 \mu\text{T}/\sqrt{\text{Hz}}$ and a spatial resolution limited by diffraction at the micrometer scale. Although much better performances can be obtained with other quantum sensors such as the N-V defect in diamond, the key advantages of the *h*-BN-based magnetic sensor described in this work are its ease of use, high flexibility and, more importantly, its ability to be placed in close proximity to a target sample. Such a sensing unit will likely find numerous applications in 2D materials research by offering a simple way to probe *in situ* the physics of van der Waals heterostructures, with optimal performance obtained for the study of nonmetallic 2D materials, for which PL quenching effects can be avoided. An improvement in magnetic sensitivity by at least one order of magnitude could be achieved by optimizing the microwave excitation used to perform ESR spectroscopy [32] while spatial resolution below the diffraction limit might be reached by relying on superresolution optical imaging methods [39–41]. To release the full potential of *h*-BN-based quantum sensing foils, however, one remaining challenge is to demonstrate that V_B^- centers can be stabilized in an atomically thin *h*-BN layer to achieve an ultimate atomic-scale proximity with the probed sample.

The data that support the findings of this study are openly available in Zenodo at <https://zenodo.org/record/6802738> with the identifier 10.5281/zenodo.6802738.

Acknowledgments.—This work was supported by the French Agence Nationale de la Recherche under the program ESR/EquipEx+ (Grant No. ANR-21-ESRE-0025), the Institute for Quantum Technologies in Occitanie through the project BONIQs, an Office of Naval Research Award No. N000142012474, and the U.S. Department of Energy, Office of Nuclear Energy under DOE Idaho Operations Office Contract DE-AC07-05ID14517 as part of a Nuclear Science User Facilities experiment. We acknowledge Abdellali Hadj-Azzem for providing the bulk $1T$ -CrTe₂ samples and the support of The Ohio State University Nuclear Reactor Laboratory and the assistance of Susan M. White, Lei Raymond Cao, Andrew Kauffman, and Kevin Herminghuysen for the irradiation services provided.

-
- [1] C. L. Degen, F. Reinhard, and P. Cappellaro, Quantum sensing, *Rev. Mod. Phys.* **89**, 035002 (2017).
 - [2] D. D. Awschalom, R. Hanson, J. Wrachtrup, and B. B. Zhou, Quantum technologies with optically interfaced solid-state spins, *Nat. Photonics* **12**, 516 (2018).

- [3] M. W. Doherty, N. B. Manson, P. Delaney, F. Jelezko, J. Wrachtrup, and L. C. Hollenberg, The nitrogen-vacancy colour centre in diamond, *Phys. Rep.* **528**, 1 (2013).
- [4] L. Rondin, J.-P. Tetienne, T. Hingant, J.-F. Roch, P. Maletinsky, and V. Jacques, Magnetometry with nitrogen-vacancy defects in diamond, *Rep. Prog. Phys.* **77**, 056503 (2014).
- [5] E. V. Levine, M. J. Turner, P. Kehayias, C. A. Hart, N. Langellier, R. Trubko, D. R. Glenn, R. R. Fu, and R. L. Walsworth, Principles and techniques of the quantum diamond microscope, *Nanophotonics* **8**, 1945 (2019).
- [6] F. Casola, T. van der Sar, and A. Yacoby, Probing condensed matter physics with magnetometry based on nitrogen-vacancy centres in diamond, *Nat. Rev. Mater.* **3**, 17088 (2018).
- [7] R. Schirhagl, K. Chang, M. Loretz, and C. L. Degen, Nitrogen-vacancy centers in diamond: Nanoscale sensors for physics and biology, *Annu. Rev. Phys. Chem.* **65**, 83 (2014).
- [8] D. R. Glenn, R. R. Fu, P. Kehayias, D. Le Sage, E. A. Lima, B. P. Weiss, and R. L. Walsworth, Micrometer-scale magnetic imaging of geological samples using a quantum diamond microscope, *Geochem. Geophys. Geosyst.* **18**, 3254 (2017).
- [9] A. Gottscholl, M. Diez, V. Soltamov, C. Kasper, D. Krauße, A. Sperlich, M. Kianinia, C. Bradac, I. Aharonovich, and V. Dyakonov, Spin defects in hBN as promising temperature, pressure and magnetic field quantum sensors, *Nat. Commun.* **12**, 4480 (2021).
- [10] J. P. Tetienne, Quantum sensors go flat, *Nat. Phys.* **17**, 1074 (2021).
- [11] A. K. Geim and I. V. Grigorieva, Van der Waals heterostructures, *Nature* **499**, 419 (2013).
- [12] T. T. Tran, K. Bray, M. J. Ford, M. Toth, and I. Aharonovich, Quantum emission from hexagonal boron nitride monolayers, *Nat. Nanotechnol.* **11**, 37 (2016).
- [13] Romain Bourrellier, Sophie Meuret, Anna Tararan, Odile Stéphan, Mathieu Kociak, Luiz H. G. Tizei, and Alberto Zobelli, Bright UV single photon emission at point defects in h-BN, *Nano Lett.* **16**, 4317 (2016).
- [14] L. J. Martínez, T. Pelini, V. Waselowski, J. R. Maze, B. Gil, G. Cassabois, and V. Jacques, Efficient single photon emission from a high-purity hexagonal boron nitride crystal, *Phys. Rev. B* **94**, 121405 (2016).
- [15] A. Sajid, M. J. Ford, and J. R. Reimers, Single-photon emitters in hexagonal boron nitride: a review of progress, *Rep. Prog. Phys.* **83**, 044501 (2020).
- [16] N. Chejanovsky, A. Mukherjee, J. Geng, Y.-C. Chen, Y. Kim, A. Denisenko, A. Finkler, T. Taniguchi, K. Watanabe, D. B. R. Dasari, P. Auburger, A. Gali, J. H. Smet, and J. Wrachtrup, Single-spin resonance in a van der Waals embedded paramagnetic defect, *Nat. Mater.* **20**, 1079 (2021).
- [17] Hannah L. Stern, Qiushi Gu, John Jarman, Simone Eizagirre Barker, Noah Mendelson, Dipankar Chugh, Sam Schott, Hoe H. Tan, Henning Sirringhaus, Igor Aharonovich, and Mete Atatüre, Room-temperature optically detected magnetic resonance of single defects in hexagonal boron nitride, *Nat. Commun.* **13**, 618 (2022).

- [18] N.-J. Guo, Y.-Z. Yang, X.-D. Zeng, S. Yu, Y. Meng, Z.-P. Li, Z.-A. Wang, L.-K. Xie, J.-S. Xu, J.-F. Wang, Q. Li, W. Liu, Y.-T. Wang, J.-S. Tang, C.-F. Li, and G.-C. Guo, Coherent control of an ultrabright single spin in hexagonal boron nitride at room temperature, (2021), [arXiv:2112.06191](https://arxiv.org/abs/2112.06191).
- [19] A. Gottscholl, M. Kianinia, V. Soltamov, S. Orlinskii, G. Mamin, C. Bradac, C. Kasper, K. Krambrock, A. Sperlich, M. Toth, I. Aharonovich, and V. Dyakonov, Initialization and read-out of intrinsic spin defects in a van der Waals crystal at room temperature, *Nat. Mater.* **19**, 540 (2020).
- [20] A. Gottscholl, M. Diez, V. Soltamov, C. Kasper, A. Sperlich, M. Kianinia, C. Bradac, I. Aharonovich, and V. Dyakonov, Room temperature coherent control of spin defects in hexagonal boron nitride, *Sci. Adv.* **7**, eabf3630 (2021).
- [21] A. J. Healey, S. C. Scholten, T. Yang, J. A. Scott, G. J. Abrahams, I. O. Robertson, X. F. Hou, Y. F. Guo, S. Rahman, Y. Lu, M. Kianinia, I. Aharonovich, and J.-P. Tetienne, Quantum microscopy with van der waals heterostructures, *Nat. Phys.* (2022).
- [22] M. Huang, J. Zhou, D. Chen, H. Lu, N. J. McLaughlin, S. Li, M. Alghamdi, D. Djugba, J. Shi, H. Wang, and C. R. Du, Wide field imaging of van der Waals ferromagnet Fe_3GeTe_2 by spin defects in hexagonal boron nitride, *Nat. Commun.* **13**, 5369 (2022).
- [23] D. C. Freitas, R. Weht, A. Sulpice, G. Remenyi, P. Strobel, F. Gay, J. Marcus, and M. Núñez-Regueiro, Ferromagnetism in layered metastable 1T-CrTe₂, *J. Phys.: Condens. Matter* **27**, 176002 (2015).
- [24] X. Sun, *et al.*, Room temperature ferromagnetism in ultra-thin van der Waals crystals of 1T-CrTe₂, *Nano Res.* **13**, 3358 (2020).
- [25] A. Purbawati, J. Coraux, J. Vogel, A. Hadj-Azzem, N. Wu, N. Bendiab, D. Jegouso, J. Renard, L. Marty, V. Bouchiat, A. Sulpice, L. Aballe, M. Foerster, F. Genuzio, A. Locatelli, T. O. Menteş, Z. V. Han, X. Sun, M. Núñez-Regueiro, and N. Rougemaille, In-plane magnetic domains and Néel-like domain walls in thin flakes of the room temperature CrTe₂ van der Waals ferromagnet, *ACS Appl. Mater. Interfaces* **12**, 30702 (2020).
- [26] F. Fabre, A. Finco, A. Purbawati, A. Hadj-Azzem, N. Rougemaille, J. Coraux, I. Philip, and V. Jacques, Characterization of room-temperature in-plane magnetization in thin flakes of CrTe₂ with a single-spin magnetometer, *Phys. Rev. Mater.* **5**, 034008 (2021).
- [27] S. Liu, R. He, L. Xue, J. Li, B. Liu, and J. H. Edgar, Single crystal growth of millimeter-sized monoisotopic hexagonal boron nitride, *Chem. Mater.* **30**, 6222 (2018).
- [28] Supplemental Material at <http://link.aps.org/supplemental/10.1103/PhysRevApplied.18.L061002> providing additional data about the magnetic field sensitivity and the heating effect, as well as a detailed description of the simulation procedure.
- [29] J. Li, E. R. Glaser, C. Elias, G. Ye, D. Evans, L. Xue, S. Liu, G. Cassabois, B. Gil, P. Valvin, T. Pelini, A. L. Yeats, R. He, B. Liu, and J. H. Edgar, Defect engineering of monoisotopic hexagonal boron nitride crystals via neutron transmutation doping, *Chem. Mater.* **33**, 9231 (2021).
- [30] A. Haykal, R. Tanos, N. Minotto, A. Durand, F. Fabre, J. Li, J. H. Edgar, V. Ivády, A. Gali, T. Michel, A. Dréau, B. Gil, G. Cassabois, and V. Jacques, Decoherence of V_B^- spin defects in monoisotopic hexagonal boron nitride, *Nat. Commun.* **13**, 4347 (2022).
- [31] A. Dréau, M. Lesik, L. Rondin, P. Spinicelli, O. Arcizet, J.-F. Roch, and V. Jacques, Avoiding power broadening in optically detected magnetic resonance of single NV defects for enhanced dc magnetic field sensitivity, *Phys. Rev. B* **84**, 195204 (2011).
- [32] X. Gao, B. Jiang, A. E. Llacsahuanga Allcca, K. Shen, M. A. Sadi, A. B. Solanki, P. Ju, Z. Xu, P. Upadhyaya, Y. P. Chen, S. A. Bhave, and T. Li, High-contrast plasmonic-enhanced shallow spin defects in hexagonal boron nitride for quantum sensing, *Nano Lett.* **21**, 7708 (2021).
- [33] W. Liu, Z.-P. Li, Y.-Z. Yang, S. Yu, Y. Meng, Z.-A. Wang, Z.-C. Li, N.-J. Guo, F.-F. Yan, Q. Li, J.-F. Wang, J.-S. Xu, Y.-T. Wang, J.-S. Tang, C.-F. Li, and G.-C. Guo, Temperature-dependent energy-level shifts of spin defects in hexagonal boron nitride, *ACS Photonics* **8**, 1889 (2021).
- [34] M. Kianinia, S. White, J. E. Fröh, C. Bradac, and I. Aharonovich, Generation of spin defects in hexagonal boron nitride, *ACS Photonics* **7**, 2147 (2020).
- [35] N.-J. Guo, W. Liu, Z.-P. Li, Y.-Z. Yang, S. Yu, Y. Meng, Z.-A. Wang, X.-D. Zeng, F.-F. Yan, Q. Li, J.-F. Wang, J.-S. Xu, Y.-T. Wang, J.-S. Tang, C.-F. Li, and G.-C. Guo, Generation of spin defects by ion implantation in hexagonal boron nitride, *ACS Omega* **7**, 1733 (2022).
- [36] J. Zhong, M. Wang, T. Liu, Y. Zhao, X. Xu, S. Zhou, J. Han, L. Gan, and T. Zhai, Strain-sensitive ferromagnetic two-dimensional Cr₂Te₃, *Nano Res.* **15**, 1254 (2022).
- [37] B. C. Buchler, T. Kalkbrenner, C. Hettich, and V. Sandoghdar, Measuring the Quantum Efficiency of the Optical Emission of Single Radiating Dipoles Using a Scanning Mirror, *Phys. Rev. Lett.* **95**, 063003 (2005).
- [38] J. Tisler, T. Oeckinghaus, R. J. Stohr, R. Kolesov, R. Reuter, F. Reinhard, and J. Wrachtrup, Single defect center scanning near-field optical microscopy on graphene, *Nano Lett.* **13**, 3152 (2013).
- [39] M. Kianinia, C. Bradac, B. Sontheimer, F. Wang, T. T. Tran, M. Nguyen, S. Kim, Z.-Q. Xu, D. Jin, A. W. Schell, C. J. Lobo, I. Aharonovich, and M. Toth, All-optical control and super-resolution imaging of quantum emitters in layered materials, *Nat. Commun.* **9**, 874 (2018).
- [40] J. Comtet, E. Glushkov, V. Navikas, J. Feng, V. Babenko, S. Hofmann, K. Watanabe, T. Taniguchi, and A. Radenovic, Wide-field spectral super-resolution mapping of optically active defects in hexagonal boron nitride, *Nano Lett.* **19**, 2516 (2019).
- [41] P. Khatri, R. N. Edward Malein, A. J. Ramsay, and I. J. Luxmoore, Stimulated emission depletion microscopy with color centers in hexagonal boron nitride, *ACS Photonics* **8**, 2081 (2021).